Modeling a Flexible Ring Net with the Discrete Element Method

Zhuo-Hui Zhu[1]; Jian-Hua Yin[2]; Chao-Jun Ouyang[3]; Dao-Yuan Tan[4]; and Jie-Qiong Qin[5]

[1]Ph.D. Candidate, Dept. of Civil and Environmental Engineering, The Hong Kong Polytechnic University, Hung Hom, Kowloon, Hong Kong, China. E-mail: zhuo-hui.zhu@connect.polyu.hk

[2]Chair Professor, Dept. of Civil and Environmental Engineering, The Hong Kong Polytechnic University, Hung Hom, Kowloon, Hong Kong, China (corresponding author). E-mail: cejhyin@polyu.edu.hk

[3]Research Associate, Institute of Mountain Hazards and Environment, Chinese Academy of Sciences, Chengdu, China. E-mail: cjouyang@imde.ac.cn

[4]Ph.D. Candidate, Dept. of Civil and Environmental Engineering, The Hong Kong Polytechnic University, Hung Hom, Kowloon, Hong Kong, China. E-mail: t.daoyuan@connect.polyu.hk

[5]Ph.D. Candidate, Dept. of Civil and Environmental Engineering, The Hong Kong Polytechnic University, Hung Hom, Kowloon, Hong Kong, China. E-mail: jieqiong.qin@connect.polyu.hk

February 2019

Abstract: Flexible barriers have been proven to be effective measures for mitigating natural hazards, such as rockfalls, gravel flows and debris flows. This paper presents a new numerical ring model based on the discrete element method (DEM) to simulate a flexible ring net. The Edinburgh Bonded Particle Model is applied to create internal forces within a ring element. The mechanical behavior of a ring element was analyzed from measurements collected during quasi-static tensile tests. The systematic calibration approach of this ring model is described in detail. Two reduction factors related to the bond Young's modulus and the bond radius are proposed to effectively adjust the bending and axial stiffnesses of the ring element. With calibrated DEM parameters from the tensile tests, the ring model is validated by reproducing these tensile tests under different boundary conditions. Finally, a three-dimensional DEM model is established for modeling the rockfall impact on a flexible ring net. A comparison between the existing test data and simulation results reveals that the new ring model can accurately reproduce the response of a flexible ring net under both static and dynamic conditions.

Author keywords: Flexible barrier; Discrete element method; Bond model; Tensile test; Rockfall.

Introduction

Flexible barriers are widely adopted in Hong Kong and many other regions and countries as protection systems against natural hazards. A flexible barrier protection system for mitigating rockfalls and debris flows consists of nets, steel ropes, brake elements and steel posts to transfer loads to foundations. In comparison with rigid barriers and other protective structures, flexible barrier protection systems are lightweight, have less of an influence on the environment, provide a considerable reduction in construction time and are also easily maintained in remote areas. A substantial amount of impact energy is dissipated through the sliding of nodes and large elastoplastic deformation of ring nets, one of the most distinguishing features of flexible barriers. In 2012, the Geotechnical Engineering Office (GEO) of The Hong Kong Special Administrative Region Government (HKSARG) produced a Discussion Note titled "Suggestions on Design Approaches for Flexible Debris-resisting Barriers" (Kwan and Cheung 2012). However, the design methods and selection of design parameters in the Discussion Note have not yet been validated. It is necessary to produce a comprehensive and recognized design standard for flexible barrier protection systems.

Over the past few decades, due to their low cost and reproducibility, numerical approaches have been developed as powerful tools for modeling flexible barriers under impact loadings of either rockfalls or debris flows. Different ring models have been developed for applications in flexible barriers (Nicot et al. 2001b; Coulibaly et al. 2017). Any type of parametric study is allowed by numerical methods; this flexibility helps to optimize a typical design. Two major approaches have been developed for modeling flexible barriers. One is the classical finite element method (FEM), which has been extensively utilized by engineers and researchers to mathematically model and numerically solve complicated structural, fluid, mechanical and electrical problems. It is essentially a mathematical method dedicated to solving partial differential equations and is well suited for modeling continuous materials. A commercial finite element code (Abaqus/Explicit), featuring nonlinear geometrical, mechanical and contact behavior in the structural dynamic range, was used to model the impact of falling rocks against common steel wire flexible meshes (Cazzani et al. 2002). Gentilini et al. (2012) proposed a highly nonlinear, dynamic, three-dimensional model that meets the requirements of major parameters in European guidelines (2008). Later, a few modifications were suggested in the model of barrier 3000 to enhance its cost-effectiveness and on-site performance (Gentilini et al. 2013). Volkvein (2004) applied newly developed discrete elements to the finite element software FARO to simulate ropes and net rings under the influence of long distance slides and included friction. Moreover, Escallón et al. (2015) developed a model that accounts for contact interactions in flexible chain-link wire nets with loose connections. Mentani et al. (2016) investigated the performance of a low-energy rockfall barrier in relation to the bullet effect based on a finite element model.

On the other hand, a more recently proposed numerical method, the discrete element method (DEM), which was initially proposed by Cundall and Strack (1979), is also capable of modeling the mechanical response of debris-resisting systems. It is the simplest discrete medium model; it adopts a particle system composed of a large number of spherical particles, meeting Newton's second law of motion and employs a spring-damper model to describe the interaction between particles. Bertrand et al. (2008, 2012) introduced a remote interaction model to simulate the double-twisted hexagonal mesh and rockfall protection fences based on the DEM under European guidelines (2008). Li and Zhao (2018) used this remote interaction model to simulate the same hexagonal-shaped wire mesh coupled with a debris mixture by using computational fluid dynamics (CFD). Thoeni et al. (2013) further improved the remote interaction model by considering distortion of the wires and hexagons. Albaba et al. (2017) established a DEM model of granular flows impacting an elementary mesh by adopting a cylindrical element (Bourrier et al. 2013).

In summary, the FEM is based on continuum mechanics theory; thus, it is appropriate to use this approach for modeling a continuous medium. However, specific algorithms are required to describe potential cracking or local failure, which is time consuming to implement. In contrast, compared to the FEM, the DEM is particularly well suited to model mechanical systems in which large relative displacements may occur during a loading process, owing to its inherent advantage in describing the granular material with particle interactions. Large displacements and failures can be easily simulated. Consequently, the DEM is suitable for modeling both flexible barriers and granular flowing materials as well as their interactions. In accordance with different materials, geometries and connection types, flexible net systems vary. However, only few bond models have been employed to simulate a simple wire mesh. A circular ring net, as a typical protection structure, has seldom been considered with the DEM due to its complex structure and special mechanical response. There is a lack of a systematic calibration process to reproduce the ring behavior both under static and dynamic conditions.

This paper presents a newly developed ring model that uses the DEM to simulate the behavior of a circular wire ring. This new ring model is developed from the Edinburgh Bonded Particle Model (EBPM) (Brown et al. 2014) based on Timoshenko beam theory with limited simplifications and assumptions. The mechanical behavior of a wire ring in a quasi-static tensile test is investigated using the new ring model. To determine the rigidity and bond strength of a wire ring, a novel calibration approach on bond parameters is elaborated based on a parametric study of tensile tests and experimental data from the literature. The model reliability is assessed by reproducing tensile tests carried out on a steel ring under different boundary conditions. Finally, the capability of the new ring model is further tested to replicate the tests results of dynamic rockfall impact on a squared ring net. This approach enables the accurate modeling of both a circular ring net and granular materials as well as their interactions in the same computational framework.

Model Description

Normally, a typical flexible barrier protection system consists of various components, such as net, supporting cables, brake elements, posts, and anchors, among which the metal wire net (Fig. 1) plays a vital role either in the mechanical behavior or in the failure mode of the entire system. A metal wire net is composed of interconnected wire rings. Hence, the behavior of a wire ring, called a ring element, under loading becomes a basic and fundamental issue. In this study, the DEM is used to simulate a ring element in EDEM software. The EBPM (Brown et al. 2014) is applied to the particles in contact to resist not only tensile and shear forces but also compressive forces and bending and twisting moments through the EDEM Application Programming Interface (API).

The EBPM, proposed by Brown at el. (2014), is based on Timoshenko beam theory that, unlike Euler-Bernoulli beam theory, accounts for the effects of transverse shear deformation. The EBPM provides a more accurate representation of true bending in a beam. Beams that are either short or have large expected deflections are more accurately modeled by considering Timoshenko beam theory.

To bond particles that are not physically in contact when using EBPM, it is necessary to set a contact radius larger than the physical radius of a particle, thus forming an overlap between two particles. Once the simulation time exceeds the bond time, the bond initialization procedure will be triggered. Particles will be bonded by a Timoshenko beam element, which links the centers of the two particles, as illustrated in Fig. 2(a). With the increase in time step, the bond forces and moments governed by the Timoshenko beam theory are updated:

$$\mathbf{\Delta F} = \mathbf{K} \cdot \mathbf{\Delta u} \tag{1}$$

where $\mathbf{\Delta F}$ is the incremental force vector, which contains 12 force and moment increments at the two ends of the bond [Fig. 2(b)]; $\mathbf{\Delta u}$ is the displacement (rotation) vector, which contains 12 displacement and rotation increments at the two ends of the bond; and $\mathbf{K}$ is a 12×12 tangential stiffness matrix, which is derived from the differential equations for beam deformation using the unit displacement theory for a Timoshenko beam. By adding all the increments since the first step of the computation, the total internal forces and moments $\mathbf{F}$ can be obtained:

$$\mathbf{F} = \sum \mathbf{\Delta F} \tag{2}$$

There are three strength criteria that determine the failure of bonds: the compressive σ_C, tensile σ_T and shear τ strength criteria. If any of the maximum stresses exceed the limit values of strength, the bond will break. The maximum compressive stress $\sigma_{C\max}$, tensile stress $\sigma_{T\max}$ and shear stress $\tau_{\max}$ are obtained by beam theory.

$$\sigma_C < \sigma_{C\max} = -\min\left(\frac{F_{qx}}{A_b} - \frac{r_b\sqrt{M_{py}^2 + M_{pz}^2}}{I_b}, \frac{F_{qx}}{A_b} - \frac{r_b\sqrt{M_{qy}^2 + M_{qz}^2}}{I_b} \right) \tag{3}$$

$$\sigma_T < \sigma_{T\max} = \max\left(\frac{F_{qx}}{A_b} + \frac{r_b\sqrt{M_{py}^2 + M_{pz}^2}}{I_b}, \frac{F_{qx}}{A_b} + \frac{r_b\sqrt{M_{qy}^2 + M_{qz}^2}}{I_b} \right) \tag{4}$$

$$\tau < \tau_{\max} = \frac{M_{px} r_b}{2I_b} + \frac{4\sqrt{F_{py}^2 + F_{pz}^2}}{3A_b} \tag{5}$$

where $A_b = \pi r_b^2$; $I_b = \frac{\pi r_b^4}{4}$. r_b is the disc radius of the bond. A_b is the cross-sectional area of the bond. I_b is the second moment of area of the bond. p and q represent the two ends of the bond. Although the bonds behave in a linear elastic brittle manner, with accurately calibrated rigidity and strength, the new ring model is capable of exhibiting large deformation consistent with the elastoplastic behavior that a metal wire ring typically experiences.

The bond elements describe the bond behavior within a ring element. For the nonbonded contact, such as the contact between the granular material and flexible ring net, the force-displacement relationship is determined by the Hertz-Mindlin contact law (Johnson 1987), which follows a spring-dashpot configuration in two directions, namely, normal and tangential (Fig. 3). The contact force is calculated by the sum of the normal force and the tangential force. Both forces include spring parts (F_{ns}; F_{ts}) and damping parts (F_{nd}; F_{td}).

The normal spring force F_{ns} is a function of normal overlap δ_n between the particles in contact and is expressed as

$$F_{ns} = \frac{4}{3} E^* \sqrt{R^*} \delta_n^{\frac{3}{2}} \tag{6}$$

where $E^* = \left(\frac{1-v_i^2}{E_i} + \frac{1-v_j^2}{E_j} \right)^{-1}$ and $R^* = \frac{R_i R_j}{R_i + R_j}$. E^* is the equivalent Young's modulus. R^* is the equivalent particle radius. E_i, R_i, v_i and E_j, R_j, v_j are the Young's moduli, Radii and Poisson's ratios of the two particles in contact. The normal damping force is given by

$$F_{nd} = -2\sqrt{\frac{5}{6}}\beta\sqrt{S_n m^*}\,\overline{v_n^{rel}} \qquad (7)$$

where $\beta = \frac{\ln e}{\sqrt{\ln^2 e + \pi^2}}$, $S_n = 2E^*\sqrt{R^*\delta_n}$, and $m^* = \frac{m_i m_j}{m_i + m_j}$. β is the damping ratio governed by the coefficient of restitution e. S_n is the normal stiffness. m^* is the equivalent mass. $\overline{v_n^{rel}}$ is the normal component of the relative velocity. m_i and m_j are the masses of each contact particle. The tangential spring force F_{ts} is based on the tangential overlap δ_t and is limited by the Coulomb friction μ. It is expressed as

$$F_{ts} = -S_t \delta_t \qquad (8)$$

where $S_t = 8G^*\sqrt{R^*\delta_n}$ and $G^* = \left(\frac{1-v_i^2}{G_i} + \frac{1-v_j^2}{G_j}\right)^{-1}$. S_t is the tangential stiffness. G^* is the equivalent shear modulus. The tangential damping force is given by

$$F_{td} = -2\sqrt{\frac{5}{6}}\beta\sqrt{S_t m^*}\,\overline{v_t^{rel}} \qquad (9)$$

where $\overline{v_t^{rel}}$ is the tangential component of the relative velocity.

Model Calibration

The quasi-static tensile test is one of the most effective ways to investigate the mechanical characteristics of a material. The bearing and deformation capacity of a ring element can be determined from such tests. Model calibration work is an essential procedure when applying the

EBPM to a flexible ring net. Once the material and deformation parameters of a ring element are determined by the test results, full-scale impact tests on flexible ring nets can proceed.

DEM Modeling of a Tensile Test

A high-grade steel wire ring net is adopted in this paper. The tested wire ring was fabricated with Al/Zn coated wires to improve corrosion resistance to extend the service life. Each ring was obtained by wrapping a single 3 mm diameter steel wire 12 times. The tested ring had a 300 mm internal diameter and was held in place by three metal clips.

In engineering practice, each ring element in a flexible ring net connects to four neighboring ring elements. Thus, there are four contact points on every ring element. A series of laboratory tests were carried out on a servo-hydraulic universal testing machine at the Swiss Federal Institute of Technology Zurich (ETHZ) (Grassl 2002). The tested ring element was mounted in a specially designed steel double plate device that can create different boundary conditions. The bolts were fixed on the holes through bushings, and the ring element was positioned in the middle of the double plates. The top double plates moved at a velocity of between 0.2 mm/s and 1 mm/s, depending on the experimental setup (Fig. 4).

The DEM modeling of a tensile test conducted in this paper is shown in Fig. 5 and is based on the same setup as that of the laboratory test in Fig. 4(a). The circular ring is discretized by bonding 100 particles to form a closed loop ring with the EBPM. Since a bond has the same circular cross-section as a wire ring, changes need to be made to the radius of the bonded particle and the bond to meet the requirements for different steel wire diameters. The cross-sectional area of a ring can be determined by the sum of the areas of the wires, but this approach will overestimate the bending stiffness of the ring. Thus, a reduction coefficient χ was introduced to calculate the equivalent cross-sectional area (A_{eq}) of a ring (Escallón and Wendeler 2013):

$$A_{eq}^{'} = \chi A_{eq} = \chi \pi r_w^2 n_w \tag{10}$$

where r_w is the radius of a wire and n_w is the number of windings. In this study, an equivalent particle radius (4.5 mm) is calculated as a reference case regardless of the value of χ. The axial and bending stiffnesses are adjusted by the bond Young's modulus and bond disc radius, which will be discussed in the following sections. The number of particles is a significant issue in the DEM simulation. As the bond is straight, as more particles are generated, the results of the ring simulation will become more accurate. The deformation of the DEM model with 100 bonded particles will be used to represent the curvature of a ring. The computational efficiency would decrease if more particles are used. Furthermore, the coefficient of bond strength variation is set to 0 to ensure that all the bonds in a ring have the same bond strength.

In addition to the bond parameters that are directly related to the tensile failure of the ring element, other values of the numerical and nonbonded contact parameters for the reference case are listed in Table 1. The global damping coefficient in the EBPM is defined as the damping applied to the particles through the equations of motion so that energy is dissipated in every particle in the system. A damping coefficient of 0.95 defines the test as a quasi-static problem, which compensates for the instability of the model induced by a relatively large loading rate (5 mm/s). Hence, a larger time step (7.87e-07) can be employed to improve the computational efficiency, and the impact of the dynamic effect can be minimized (Cho et al. 2007).

Fig. 6 depicts the four stages of the quasi-static tensile test of a 300 mm diameter ring element fixed at 4 vertices of contact:

(a) Bonds are generated between particles at the bond time. Then, the steel plates move at a certain velocity, and forces act on the ring through the four bolts.

(b) The ring deforms nonlinearly due to the change in geometry, which represents the bending behavior of the ring.

(c) The ring is stretched into a rectangular shape, and geometric nonlinearity no longer occurs. The forces increase faster in this stage than they did in the second stage. The bearing capacity is determined mainly by the normal force in the ring.

(d) The deformation of the ring increases with loading until a bond is broken and the ring fails.

Parametric Study on the Bond Parameters of the Tensile Test Simulations

For the purpose of simulating a specific ring element, the relationship between the DEM parameters and failure criteria should be studied. The influences of the three most important bond parameters, bond Young's modulus, mean bond tensile strength and bond radius multiplier, are investigated by analyzing the force-deformation characteristics, breaking load and maximum deformation of a ring element. Other nonbonded contact parameters are not considered to have a significant influence on the failure mode of a ring. The ranges of the values used in the parametric study are shown in Table 2.

Effects of the Bond Young's Modulus

Fig. 7(a) plots the effects of the bond Young's modulus (E_b) on the load-displacement relationship of the ring. The range of the bond Young's modulus is from 40 GPa to 200 GPa. With the increase in the bond Young's modulus, the bonds become stiffer. Thus, to produce the same deformation of the ring, a greater applied loading force is needed to resist the induced bond forces. For a ring with a 200 GPa bond Young's modulus, the ring breaks during the shape-changing stage. Fig. 7(b and c) show the respective relations between the bond Young's modulus and the breaking load and maximum elongation at failure. Because the value of the bond Young's modulus modifies the stiffness of the bond, considerable elongation occurs when the bond Young's modulus decreases to 40 GPa, which is more than three times that when the bond Young's modulus is 200 GPa. A significant increase in loading is observed accordingly.

Effects of the Mean Bond Tensile Strength

Fig. 8 shows the effects of the mean bond tensile strength (T_s) on the load-displacement relationship, breaking load and maximum elongation of a ring. The tested mean bond tensile strengths range from 4 GPa to 20 GPa and the bond Young's modulus is 120 GPa. The load-displacement curves of the 5 tests nearly overlap due to the identical stiffness of the rings. Generally, the breaking load and maximum elongation increase with the mean bond tensile strength. Linear relations are observed after the ring is stretched into a rectangular shape. During this stage, the bond force is mainly affected by the properties of the material itself, rather than the geometrical deformation.

Effects of the Bond Radius Multiplier

The bond radius multiplier λ is a reduction coefficient of the bond radius that can influence the bond stiffness and strength:

$$r_b = \lambda \min(r_A, r_B) \tag{11}$$

where r_A and r_B are the radii of particles A and B, respectively. Fig. 9 demonstrates the effects of the bond radius multiplier on the load-displacement relationship, breaking load and maximum elongation of a ring. The range of the bond radius multiplier is from 0.5 to 0.9. The bond radius multiplier has a significant influence on the breaking load because it changes the cross-sectional area of the bond. For a given mean bond tensile strength, the bond force and stiffness decrease with the decreasing cross-sectional area. Therefore, the bond becomes more ductile as the bond radius multiplier decreases. The maximum elongation will slightly increase. However, the effects of the bond radius multiplier on the maximum elongation are less significant in contrast with the results of varying the bond Young's modulus.

Rigidity and Bond Strength Determination of a Ring Element

The reference case of the quasi-static tensile test reveals that the bending and axial stiffnesses of the ring dominate the ring element behavior in different stages. Notably, the equivalent particle radius (r_{eq}) of 4.5 mm was determined based on the actual cross-section of a circular ring and the particle number of a ring element in the simulation. The equivalent particle radius did not equal the equivalent bond radius (R_{eq}), which affects the stiffness of a ring element. The bending stiffness can be expressed as

$$k_{bending} = EI = E\frac{\pi R_{eq}^4}{4} \tag{12}$$

where $R_{eq} = \sqrt{\frac{A_{eq}}{\pi}} = \sqrt{r_w^2 n_w} = \lambda r_{eq}$. E is the steel Young's modulus (200 GPa). The axial stiffness can be expressed as

$$k_{axial} = EA = E\pi R_{eq}^2 \tag{13}$$

Grassl (2002) found that the theoretical axial stiffness is five times the rigidity in the tensile test for wire rings with 7, 12 and 19 turns. This should be explained by the different utilization of the individual wires because the axial stiffness k decreases with the increased loading for a single wire tensile test. The overall axial stiffness of a wire ring is the sum of the individual wires connected in parallel. Therefore, the sum of the axial stiffness should be less than $n_w k$ and the axial stiffness can be rewritten as

$$k_{axial} = \frac{1}{5} E\pi r_w^2 n_w \tag{14}$$

As mentioned in the proceeding sections, the bending stiffness should be reduced to eliminate the overestimation of the area moment of inertia by decreasing the equivalent bond radius. However, according to Eq. (13), the axial stiffness will decrease with the bond radius; this result is consistent with the parametric study. The reduction of the bond radius cannot change the bending and axial stiffnesses independently. Based on the equations and findings from the parametric study, the bond Young's modulus can likewise influence the bending and axial stiffnesses; thus, two coefficients γ and η, are inserted into Eq. (12) and Eq. (13):

$$k_{bending} = \eta E \frac{\pi(\gamma R_{eq})^4}{4} \tag{15}$$

$$k_{axial} = \eta E \pi (\gamma R_{eq})^2 \tag{16}$$

where $\gamma R_{eq} = \lambda r_{eq}$. Substitution of Eq. (14) into Eq. (16) gives the reduction factor of the axial stiffness:

$$\eta\gamma^2 = \frac{1}{5} \tag{17}$$

γ and η can be easily obtained by Eq. (17) once the reduction factor of bending stiffness ($\eta\gamma^4$) is known. $\eta\gamma^4$ can be determined by assuming $\eta = 1$ and testing different values of λ until reaching a good agreement with the experimental bending response.

The experiment (Grassl 2002) related to the ring with 4 vertices of contact is employed for model calibration. Finally, the bond Young's modulus, bond tensile strength and bond radius multiplier were calibrated by fitting the experimental and DEM results (Fig. 10). There is a slight difference between these sets of results in the final stage of the test. The fluctuation in the physical test may be explained by the incompatible deformation of the individual wires and the slip between the wire and clips, whereas the DEM model cannot account for these effects. The results are also compared to the FEM predictions by Grassl (2002). The FEM ring element was developed and implemented in the FARO finite element program. The resistance due to bending and traction for any boundary conditions are detected with 8 bar and 8 spring elements. Our new ring model exhibits a better fit in the tensile regime than that of the FEM result. The values of the DEM parameters of the ring tensile test are listed in Table 3.

Model Validation

Modeling of Tensile Tests with Different Boundary Conditions

To validate the calibrated parameters of the ring model, two additional DEM tensile tests of the same 300 mm diameter ring element with 2 and 3 vertices of contact were conducted. The obtained load-displacement relationship is compared to the corresponding experimental data and FEM results (Grassl 2002), as shown in Fig. 11(a and b). The bending stiffness is slightly underestimated for both cases, mainly attributable to the constant change in the cross-sectional area of the ring in the bending regime. Different area moments of inertia shall lead to different bending stiffnesses. In addition, because the ring model is not able to consider plastic deformation in the bending regime, the ring will enter the tensile regime slightly earlier than in the experiment.

Furthermore, a more complex loading condition with a group of 8 interconnected wire rings [Fig. 4(d)] was considered to account for the ring net response. The DEM predictions agree with the experimental results, matching the net response in both the bending and tensile regimes [Fig. 11(c)]. The ring model exhibits a better performance in describing the axial resistance of the group wire rings than that of the FEM model. Sudden drops in loading occur in the tensile regime due to the sliding motion between the wire rings in contact.

Owing to the proper calibration of parameters and the inherent advantage of the ring model in dealing with geometrical nonlinearity, the model response is quite agreeable to the results of the experiment in various loading configurations. Therefore, further study of the entire flexible ring net can be carried out on the basis of the new ring model.

Modeling of Rockfall Impact Tests on a Flexible Ring Net

Based on the tensile test results of the ring element, the overall performance and dynamic response of the flexible ring net is evaluated by a falling rock impact test. The experimental test was conducted at the Swiss Federal Rockfall Test Site in Walenstadt (SG), Switzerland (Grassl 2002). The test ring net employed was composed of the same 300 mm diameter rings as the tensile test in the above section. Each ring is linked with four others. A total of 180 ring elements constitute the net with dimensions of 3.9 m × 3.9 m. The net was fixed to the top of a rigid steel frame by shackles. A boulder of mass 825 kg was lifted to 3 m above the net and dropped with 24.3 kJ of kinetic energy [Fig. 12(a)]. In parallel to the experiment, an FEM model (Grassl 2002) was built to simulate the rockfall tests. The aforementioned FEM ring element was used to describe the wire net behavior. For each ring, 8 nodes are used to connect the bar elements and detect the contact points of adjacent rings and rockfall material.

By making use of the experimental data, a full-scale three-dimensional DEM model was established to validate the test and obtain a better understanding of the interaction between the rockfall and flexible ring net. For a real flexible ring net, the connection points between the rings is moveable, which allows the ring elements to slide during the impact. To accurately simulate the behavior of the ring net, 180 ring elements formed by 18000 particles were generated in three-dimensional space through the EDEM API [Fig. 12(b)]. In the stage of particle generation, each ring was rotated to an appropriate degree to avoid contact with the other rings. Bonds were created between only adjacent particles within each ring. In addition, boundary conditions represented by rigid steel rings were added to the outermost rings, allowing rotation and sliding of the rings. A spherical boulder was released from the same height to the net as that in the physical test. Moreover, since the ring net is influenced by gravitational acceleration, it is necessary to consider the initial sag of the net by allowing the net to fall to a free state before boulder impact.

Fig. 13 displays the three-dimensional lateral view of the net deformation developed during the impact test at different time points. Fig. 14(a) depicts the evolution with time of the rockfall acceleration, in comparison with the test data and FEM results. Time 0 corresponds to the first contact of the boulder with the net. This result indicates a good correlation between the experimental results and the DEM simulation. The acceleration of the boulder in the DEM model increases slightly faster than that in the experiment from time 0.1 s to time 0.15 s. The distinct initial states of the interconnected wire rings between the model and experiment may lead to this difference, although the initial sag of the net was taken into account. In accordance with the calibration procedures, impact tests were repeatedly performed for different sizes of wire rings with 7 and 19 turns to further evaluate the reliability of the ring model [Fig. 14(b and c)]. It is observed that the maximum acceleration of the boulder decreases with an increasing number of turns. In contrast to the FEM results, the developed DEM ring model with less oscillations is more accurate for predicting the dynamic response of a flexible ring net under rockfall impact.

Summary and Findings

In this paper, the Edinburgh Bonded Particle Model (EBPM) is employed to establish a new numerical ring model for a steel wire ring. The effects of the bond parameters of this ring element are investigated by means of a series of parametric studies in modeling quasi-static tensile tests. The rigidity and bond strength of the ring model are carefully calibrated. In addition, the ring model is validated by comparing computed values with test data. A three-dimensional discrete element method (DEM) model for a flexible ring net is developed and applied for simulating the deformation of a flexible ring net under the impact of a falling rock. Based on these works, the following findings are obtained:

1. The new numerical ring model for a steel wire ring (a ring element) based on the EBPM is suitable for modeling a steel wire ring.
2. The calibration of bond parameters in this new ring model can be easily performed by comparing the modeling values with available test data.
3. The three-dimensional DEM flexible ring net based on our new ring model can reproduce the behavior of a ring net barrier under rockfall impact, allowing engineers to employ this model as a design tool of this typical structure. Furthermore, the model also has great potential in the

study of the interaction between flexible barriers and other natural hazards, including gravel flows and debris flows in the same framework due to the inherent merits in describing particle interactions by the DEM. The proposed DEM model will enable parametric studies on the interaction between flexible barriers and natural hazards under more complicated impact loading conditions.

4. Compared with finite element modeling of a ring net, any simplified fine-mesh modes composed of truss or spring elements are not necessarily established in a discrete element model. It is more accurate to describe the behavior of both a single ring element and an entire flexible ring net under impact loadings with the DEM than the FEM. Other deformable components, such as steel cables and brake elements, can be added into our DEM model to evaluate the performance of a whole flexible ring net barrier system under impact loadings.

It is recommended that large-scale physical model impact tests related to rockfalls and debris flows be executed to compare and validate the proposed numerical DEM model with new ring elements in the future.

Acknowledgements

The authors would like to thank Professor Jin Ooi from the University of Edinburgh for providing the source code of the Bonded Particle Model on updating and Professor Jian-Fei Chen of Queen's University Belfast for advising us on the bond modeling and DEM modeling. The authors acknowledge the financial support from Research Institute for Sustainable Urban Development of The Hong Kong Polytechnic University (PolyU). The work in this paper is also supported by a National State Key Project "973" grant (Grant No.: 2014CB047000) (sub-project No.

2014CB047001) from Ministry of Science and Technology of the People's Republic of China, a CRF project (Grant No.: PolyU12/CRF/13E) from Research Grants Council (RGC) of Hong Kong Special Administrative Region Government of China. The financial supports from PolyU grants (1-ZVCR. 1-ZVEH. 4-BCAU, 4-BCAW, 4-BCB1, 5-ZDAF) are acknowledged. This paper is also supported by Research Centre for Urban Hazards Mitigation of Faculty of Construction and Environment of PolyU.

References

Albaba, A., Lambert, S., Kneib, F., Chareyre, B., and Nicot, F. (2017). “DEM modeling of a flexible barrier impacted by a dry granular flow.” Rock Mechanics and Rock Engineering., 50(11), 3029-3048.

Bertrand, D., Nicot, F., Gotteland, P., and Lambert, S. (2008). “Discrete element method (DEM) numerical modeling of double-twisted hexagonal mesh.” Canadian Geotechnical Journal., 45(8), 1104-1117.

Bertrand, D., Trad, A., Limam, A., and Silvani, C. (2012). “Full-scale dynamic analysis of an innovative rockfall fence under impact using the discrete element method: from the local scale to the structure scale.” Rock mechanics and rock engineering., 45(5), 885-900.

Bourrier, F., Kneib, F., Chareyre, B., and Fourcaud, T. (2013). “Discrete modeling of granular soils reinforcement by plant roots.” Ecological Engineering., 61, 646-657.

Brown, N. J., Chen, J. F., and Ooi, J. Y. (2014). “A bond model for DEM simulation of cementitious materials and deformable structures.” Granular Matter., 16(3), 299-311.

Cazzani, A., Mongiovı, L., and Frenez, T. (2002). “Dynamic finite element analysis of interceptive devices for falling rocks.” International Journal of Rock Mechanics and Mining Sciences., 39(3), 303-321.

Cho, N. A., Martin, C. D., and Sego, D. C. (2007). “A clumped particle model for rock.” International Journal of Rock Mechanics and Mining Sciences., 44(7), 997-1010.

Coulibaly, J. B., Chanut, M. A., Lambert, S., and Nicot, F. (2017). “Nonlinear discrete mechanical model of steel rings.” Journal of Engineering Mechanics., 143(9), 04017087.

Cundall, P. A., and Strack, O. D. (1979). "A discrete numerical model for granular assemblies." Geotechnique., 29(1), 47-65.

Escallón, J. P., and Wendeler, C. (2013). "Numerical simulations of quasi-static and rockfall impact tests of ultra-high strength steel wire-ring nets using Abaqus/Explicit." In 2013 SIMULIA Community conference.

Escallón, J. P., Wendeler, C., Chatzi, E., and Bartelt, P. (2015). "Mechanics of chain-link wire nets with loose connections." Engineering Structures., 101, 68-87.

ETAG, EOTA. (2008). "027-Guideline for European technical approval of falling rock protection kits." Eur Organisat Techn Appr.

Gentilini, C., Gottardi, G., Govoni, L., Mentani, A., and Ubertini, F. (2013). "Design of falling rock protection barriers using numerical models." Engineering Structures., 50, 96-106.

Gentilini, C., Govoni, L., de Miranda, S., Gottardi, G., and Ubertini, F. (2012). "Three-dimensional numerical modelling of falling rock protection barriers." Computers and Geotechnics., 44, 58-72.

Grassl, H. G. (2002). "Experimentelle und numerische Modellierung des dynamischen Trag-und Verformungsverhaltens von hochflexiblen Schutzsystemen gegen Steinschlag" PhD. thesis, ETH Zurich, Zurich, Switzerland (in German).

Johnson, K. L. (1987). "Contact mechanics." Cambridge university press., Cambridge.

Kwan, J. S. H., and Cheung, R. W. M. (2012). "Suggestion on design approaches for flexible debris-resisting barriers. Standard and testing division." Discussion note DN1/2012. The Government of Hong Kong Special Administrative Region.

Li, X., and Zhao, J. (2018). “A unified CFD-DEM approach for modeling of debris flow impacts on flexible barriers.” International Journal for Numerical and Analytical Methods in Geomechanics.

Mentani, A., Giacomini, A., Buzzi, O., Govoni, L., Gottardi, G., and Fityus, S. (2016). “Numerical modelling of a low-energy rockfall barrier: new insight into the bullet effect.” Rock Mechanics and Rock Engineering., 49(4), 1247-1262.

Nicot, F., Cambou, B., and Mazzoleni, G. (2001b). “From a constitutive modelling of metallic rings to the design of rockfall restraining nets.” International Journal for Numerical and Analytical Methods in Geomechanics., 25(1), 49-70.

Thoeni, K., Lambert, C., Giacomini, A., and Sloan, S. W. (2013). “Discrete modelling of hexagonal wire meshes with a stochastically distorted contact model.” Computers and Geotechnics., 49, 158-169.

Volkwein, A. (2004). “Numerische simulation von flexiblen steinschlagschutzsystemen.” PhD. thesis, ETH Zurich, Zurich, Switzerland (in German).

Table 1. Values of DEM Parameters for the Reference Case of a Quasi-Static Tensile Test

DEM Parameters	**Values**
Bond	
Bond Young's modulus (GPa)	120
Bond Poisson's ratio	0.3
Compressive strength (GPa)	16
Tensile strength (GPa)	16
Shear strength (GPa)	10
Coefficient of variation of the strength	0
Bond radius multiplier	0.8
Non-bond	
Particle radius (mm)	4.5
Particle contact radius (mm)	8
Particle density (kg/m^3)	7800
Particle Young's modulus (GPa)	200
Particle Poisson's ratio	0.3
Coefficient of static friction	1
Coefficient of rolling friction	0
Coefficient of restitution	0.5
Numerical	
Loading rate v (m/s)	0.005
Global damping coefficient	0.95
Time step (s)	7.87e-07

Table 2. Parametric Study on Bond Parameters of a Quasi-Static Tensile Test

Parameters	**Refence**	**Min**	**Max**
Bond Young's modulus (GPa)	120	40	200
Mean bond tensile strength (GPa)	16	4	20
Bond radius multiplier	0.8	0.5	0.9

Table 3. Calibrated Bond Parameters for a 300mm Flexible Ring Element

Parameters	**Values**
Bond Young's modulus (GPa)	292
Bond Poisson's ratio	0.3
Tensile strength (GPa)	41
Shear strength (GPa)	12
Coefficient of variation of the strength	0
Bond radius multiplier	0.43

Fig 1

Fig 2

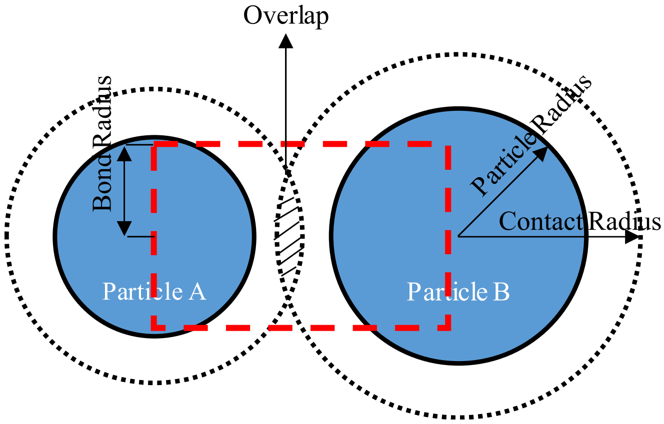
Overlap
Bond Radius
Particle Radius
Contact Radius
Particle A
Particle B

(a)

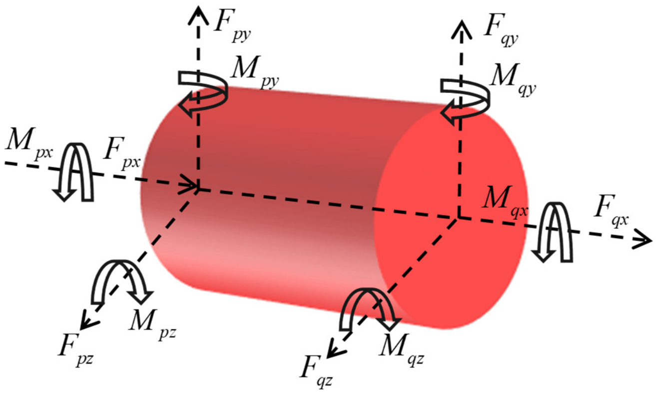
F_{py}
M_{py}
F_{qy}
M_{qy}
M_{px}
F_{px}
M_{qx}
F_{qx}
M_{pz}
F_{pz}
M_{qz}
F_{qz}

(b)

Fig 3

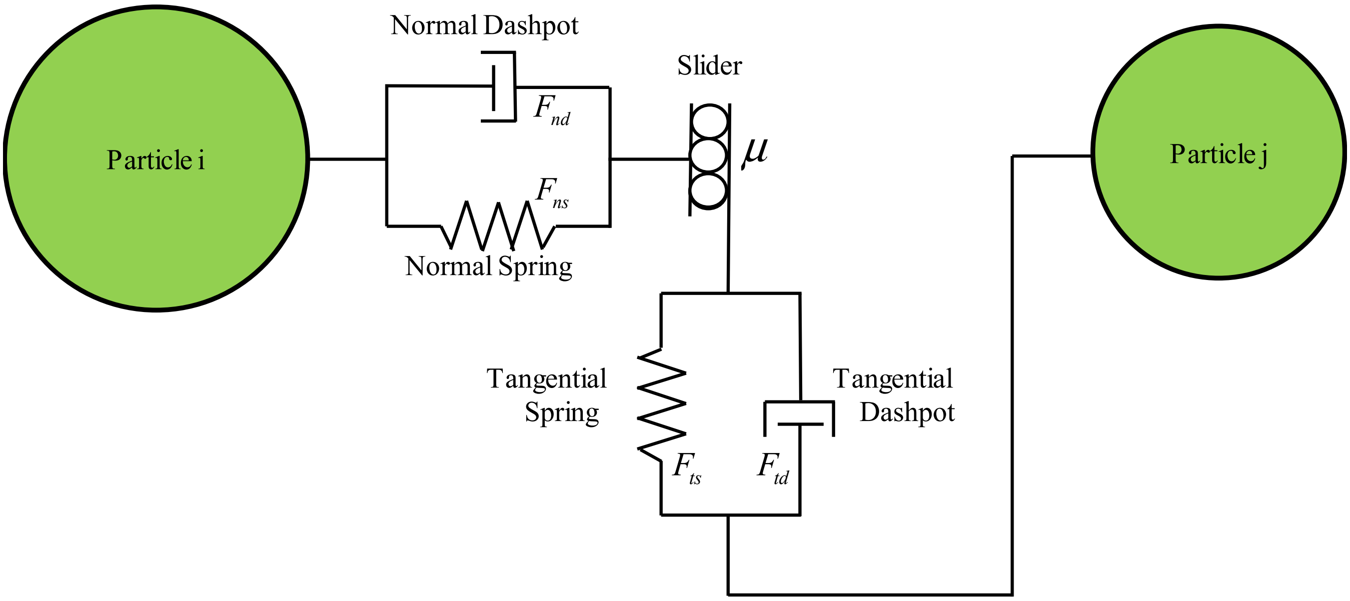

Normal Dashpot
Slider
F_{nd}
μ
Particle i
Particle j
F_{ns}
Normal Spring
Tangential
Spring
Tangential
Dashpot
F_{ts}
F_{td}

Fig 4

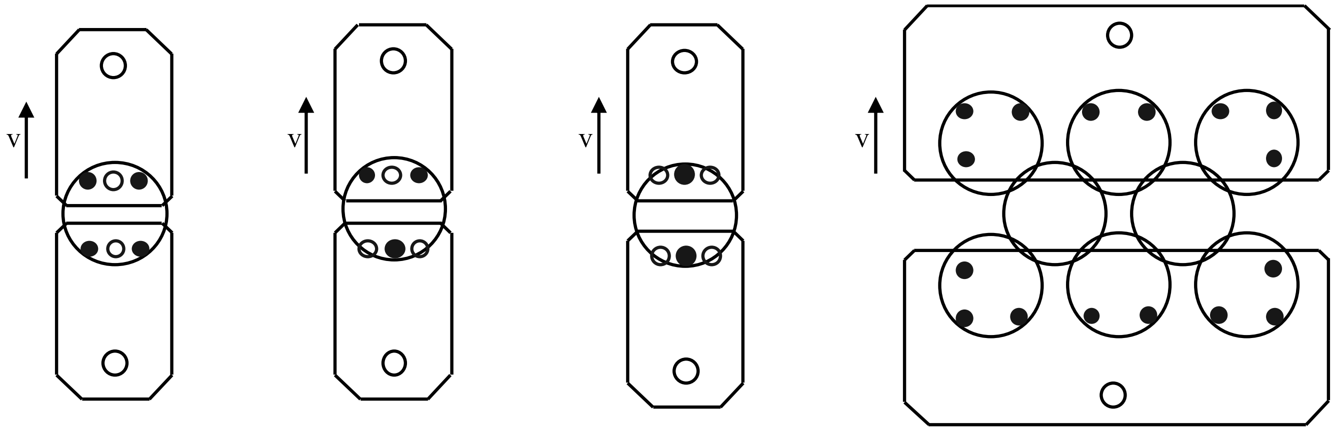

(a) (b) (c) (d)

Fig 5

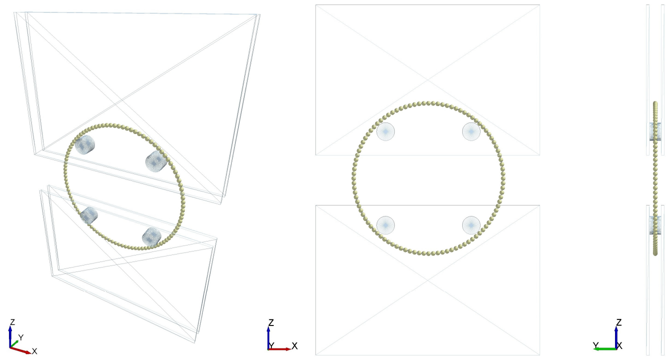

Fig 6

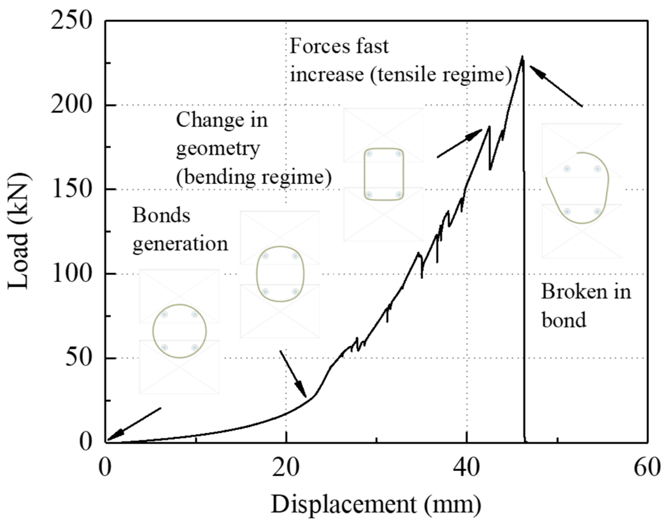

250
200
150
100
50
0
0
20
40
60
Load (kN)
Displacement (mm)
Bonds generation
Change in geometry (bending regime)
Forces fast increase (tensile regime)
Broken in bond

Fig 7

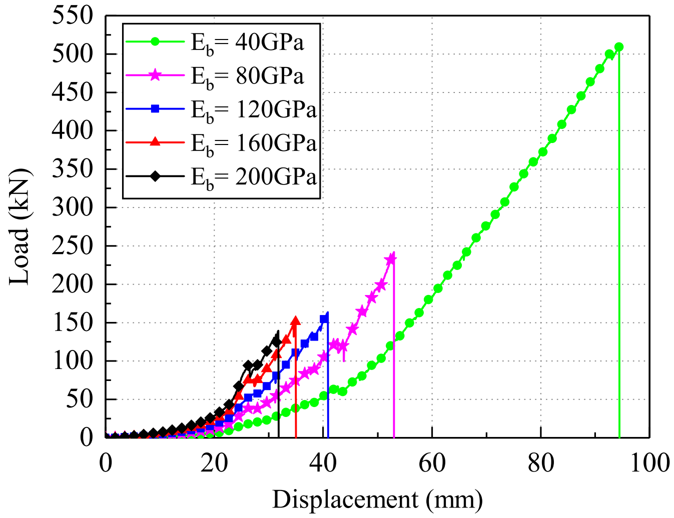

Load (kN)
Displacement (mm)
E_b= 40GPa
E_b= 80GPa
E_b= 120GPa
E_b= 160GPa
E_b= 200GPa

(a)

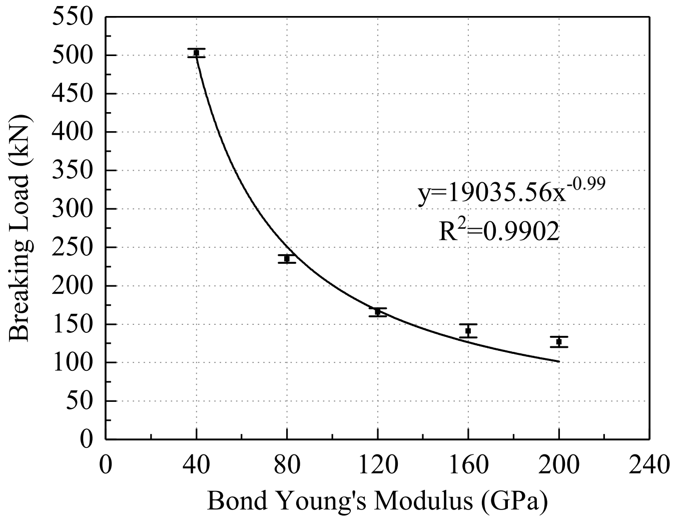

Breaking Load (kN)
Bond Young's Modulus (GPa)
$y=19035.56x^{-0.99}$
$R^2=0.9902$

(b)

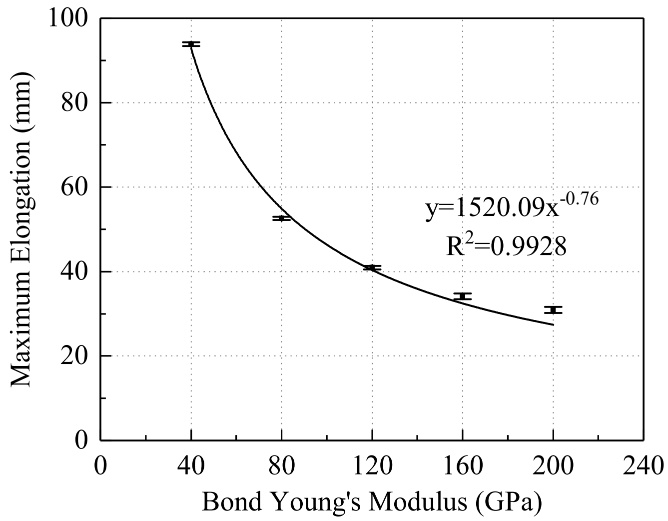

Maximum Elongation (mm)
Bond Young's Modulus (GPa)
$y=1520.09x^{-0.76}$
$R^2=0.9928$

(c)

Fig 8

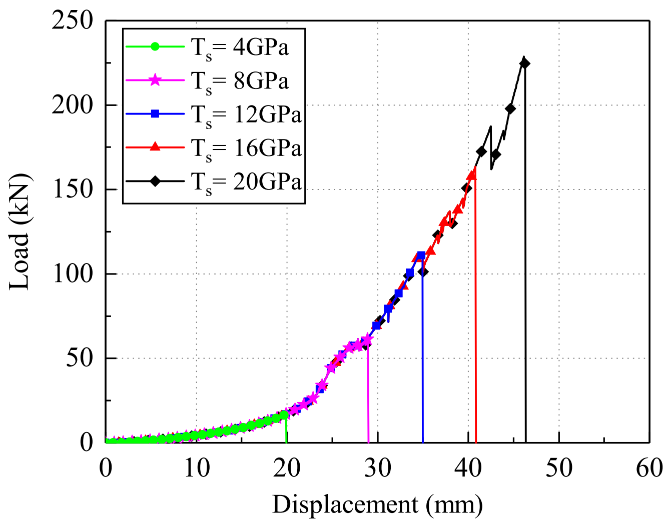

Load (kN)
Displacement (mm)
0
50
100
150
200
250
0
10
20
30
40
50
60
T_s= 4GPa
T_s= 8GPa
T_s= 12GPa
T_s= 16GPa
T_s= 20GPa

(a)

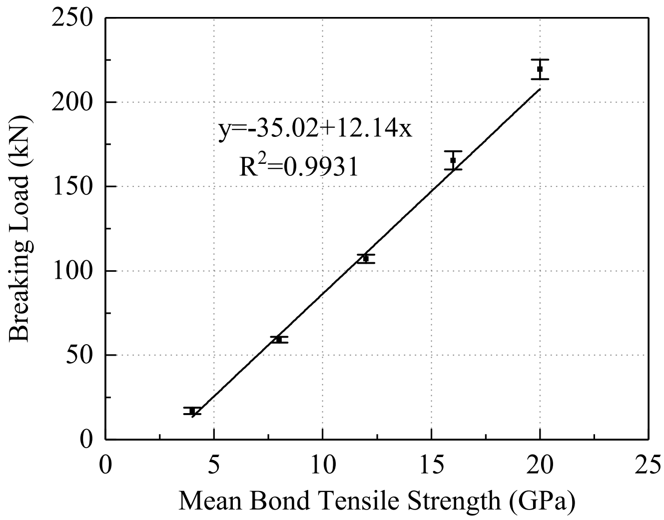

Breaking Load (kN)
Mean Bond Tensile Strength (GPa)
0
50
100
150
200
250
0
5
10
15
20
25
y=-35.02+12.14x
R2=0.9931

(b)

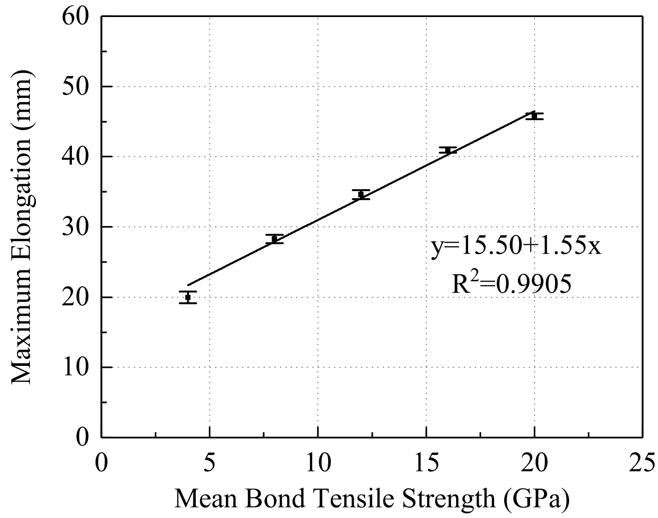

Maximum Elongation (mm)
Mean Bond Tensile Strength (GPa)
0
10
20
30
40
50
60
0
5
10
15
20
25
y=15.50+1.55x
R2=0.9905

(c)

Fig 9

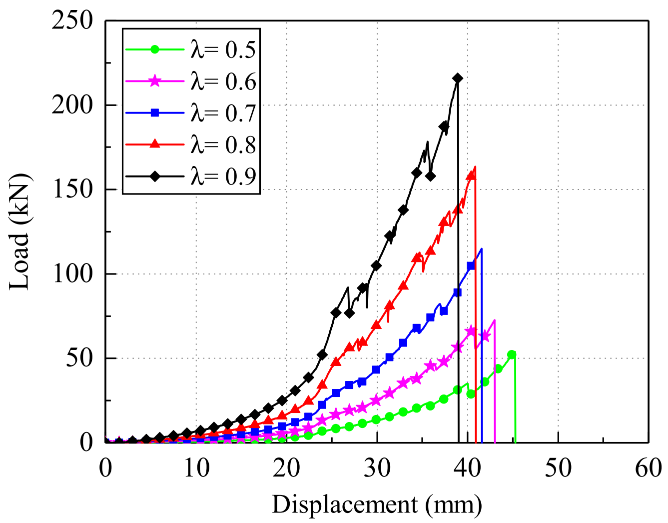

Load (kN)
Displacement (mm)
λ= 0.5
λ= 0.6
λ= 0.7
λ= 0.8
λ= 0.9

(a)

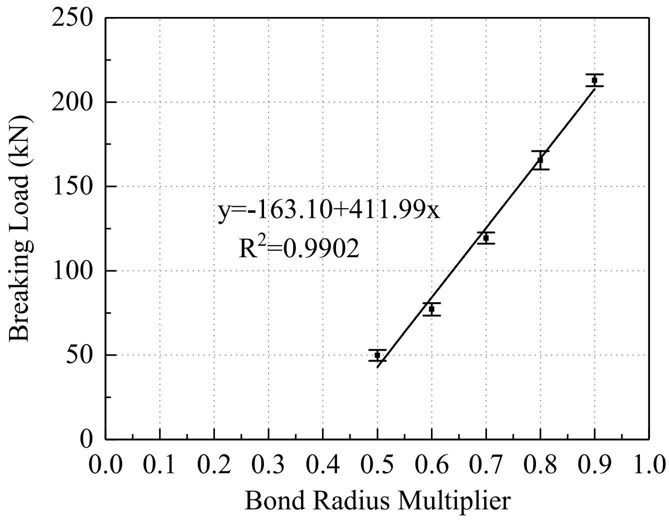

Breaking Load (kN)
Bond Radius Multiplier
y=-163.10+411.99x
R2=0.9902

(b)

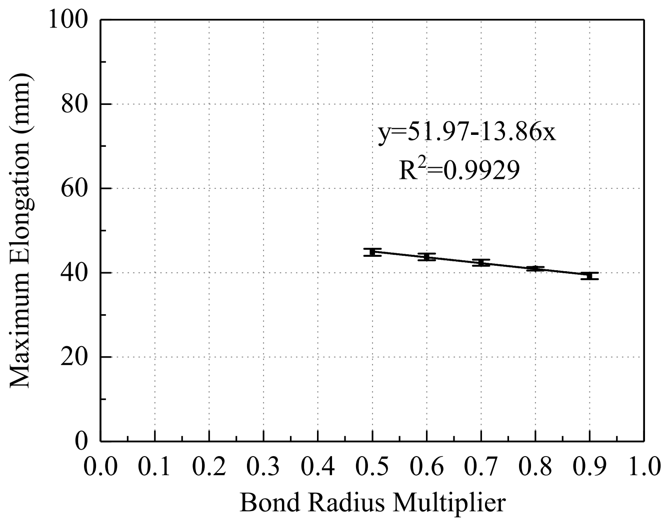

Maximum Elongation (mm)
Bond Radius Multiplier
y=51.97-13.86x
R2=0.9929

(c)

Fig 10

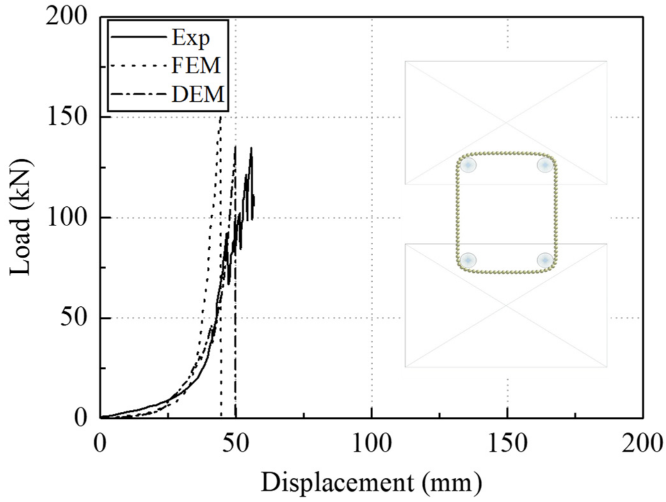

Exp
FEM
DEM
Load (kN)
Displacement (mm)
200
150
100
50
0
0
50
100
150
200

Fig 11

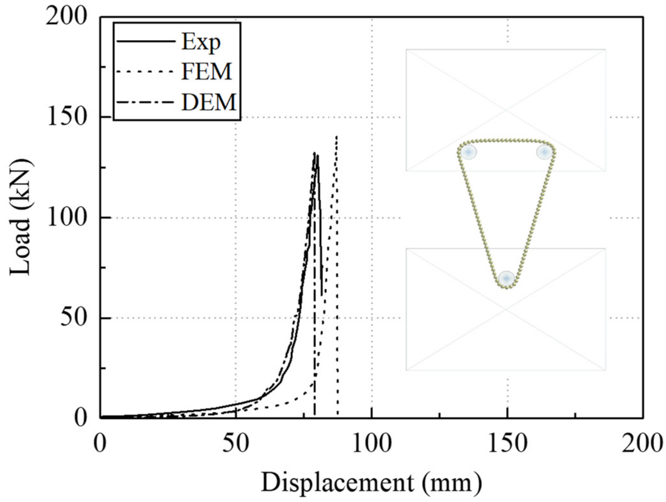
Exp
FEM
DEM
Load (kN)
Displacement (mm)
0
50
100
150
200
0
50
100
150
200

(a)

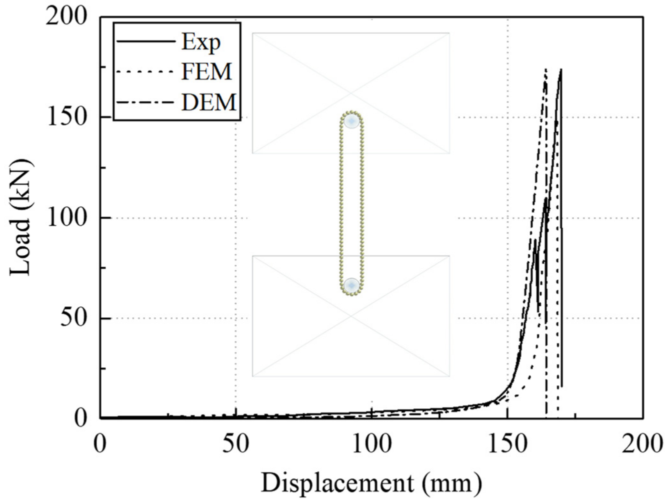
Exp
FEM
DEM
Load (kN)
Displacement (mm)
0
50
100
150
200
0
50
100
150
200

(b)

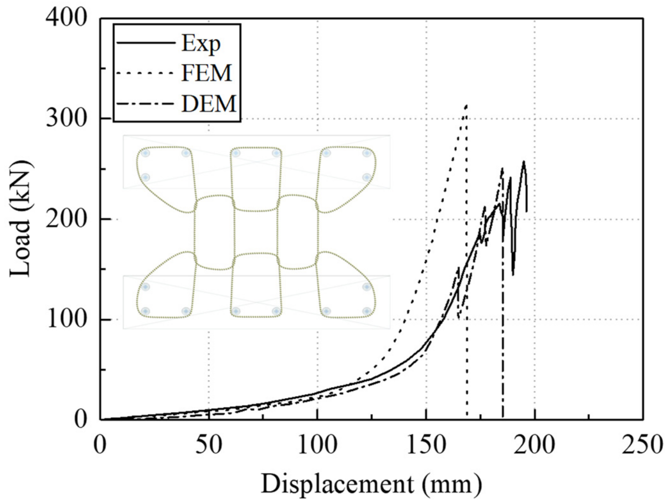
Exp
FEM
DEM
Load (kN)
Displacement (mm)
0
100
200
300
400
0
50
100
150
200
250

(c)

Fig 12

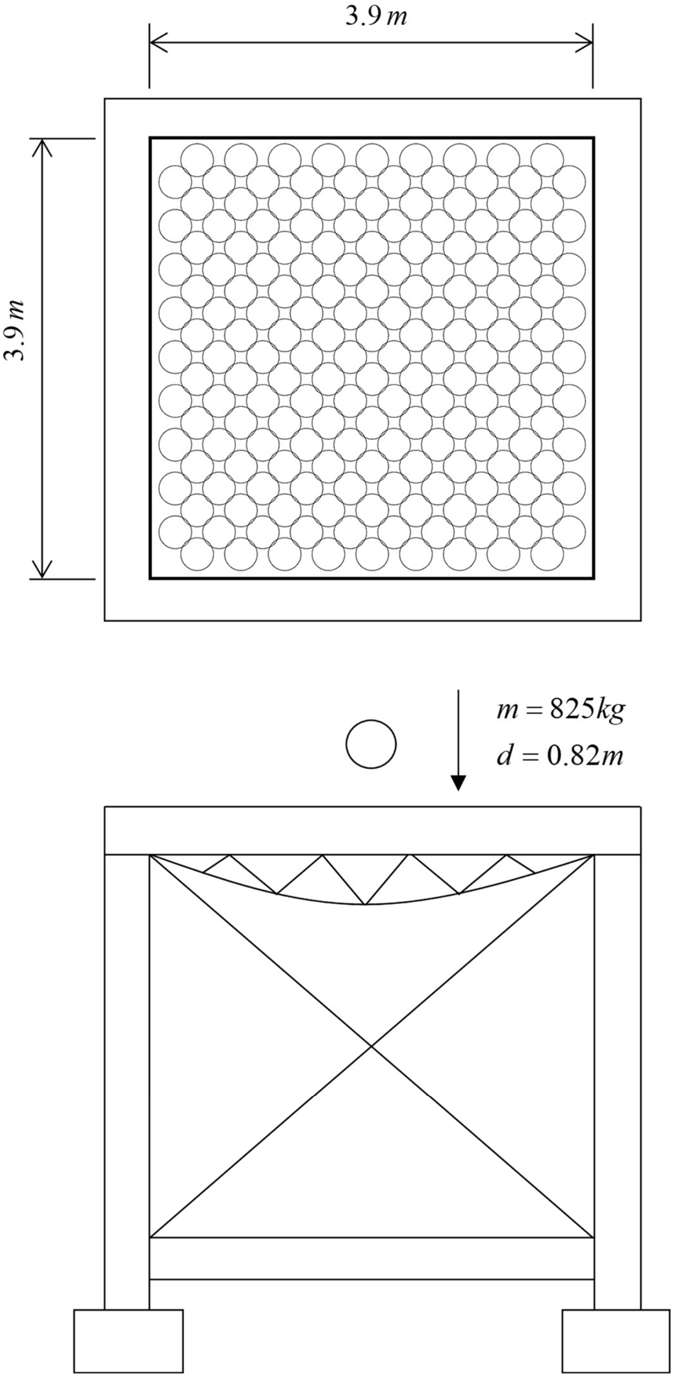

(a)

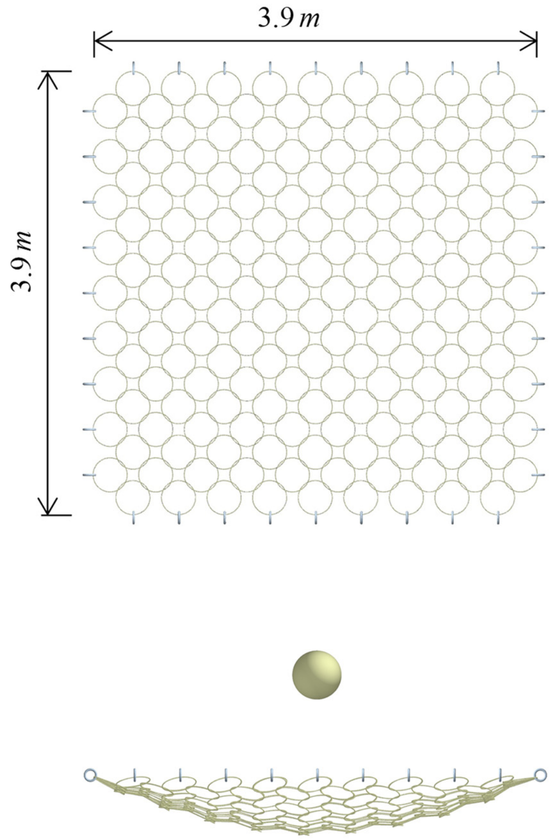

(b)

Fig 13

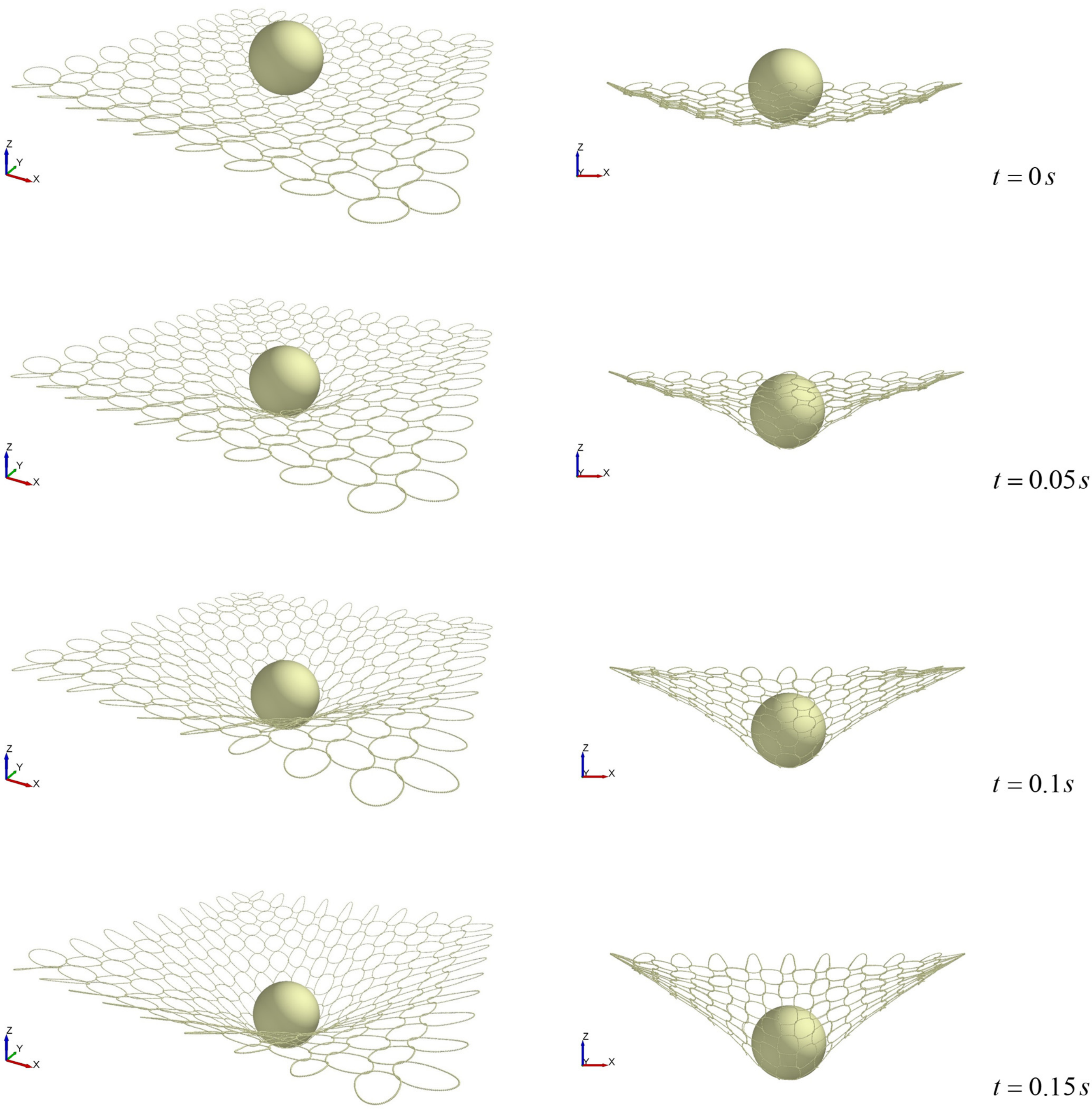

Fig 14

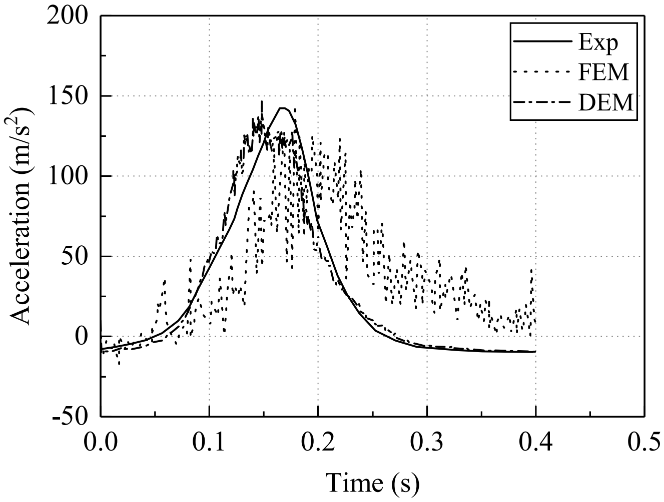
Exp
FEM
DEM
Acceleration (m/s^2)
Time (s)
200
150
100
50
0
-50
0.0
0.1
0.2
0.3
0.4
0.5

(a)

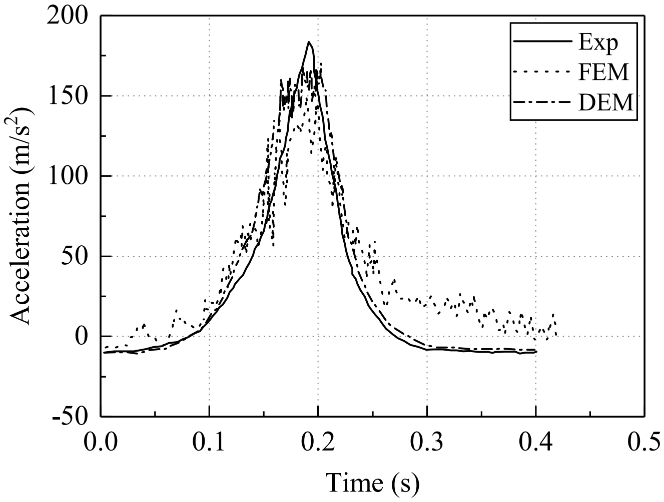
Exp
FEM
DEM
Acceleration (m/s^2)
Time (s)
200
150
100
50
0
-50
0.0
0.1
0.2
0.3
0.4
0.5

(b)

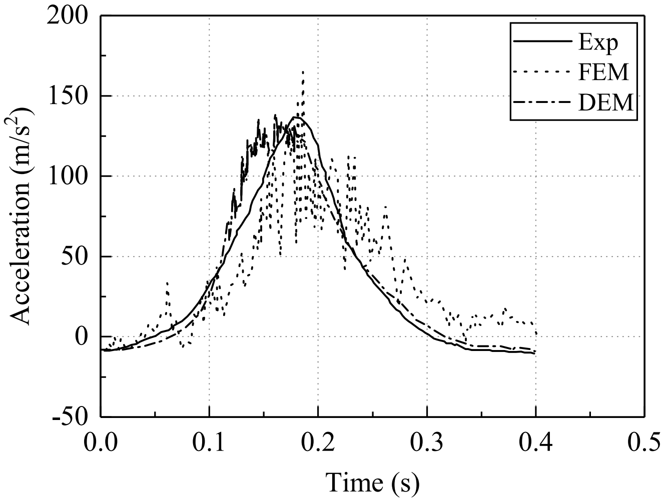
Exp
FEM
DEM
Acceleration (m/s^2)
Time (s)
200
150
100
50
0
-50
0.0
0.1
0.2
0.3
0.4
0.5

(c)

Figure Caption List

Fig. 1. Flexible metallic wire ring net in Hong Kong

Fig. 2. Two particles bonded by a Timoshenko beam element

Fig. 3. Schematic of the Hertz-Mindlin contact model

Fig. 4. Quasi-static tensile tests with 300 mm diameter steel ring elements: (a) 4 vertices of contact; (b) 3 vertices of contact; (c) 2 vertices of contact; (d) a group of 8 wire rings

Fig. 5. The DEM model of a quasi-static tensile test

Fig. 6. Four stages of the reference case tensile test

Fig. 7. Effects of the bond Young's modulus on (a) load-displacement relationship; (b) breaking load; (c) maximum elongation

Fig. 8. Effects of the mean bond tensile strength on (a) load-displacement relationship; (b) breaking load; (c) maximum elongation

Fig. 9. Effects of the bond radius multiplier on (a) load-displacement relationship; (b) breaking load; (c) maximum elongation

Fig. 10. Comparison of DEM simulation values with FEM and experimental results of a tensile test with a 300 mm diameter steel ring element (4 vertices of contact)

Fig. 11. Comparison of DEM simulation values with FEM and experimental results of a tensile test with a 300 mm diameter steel ring element: (a) 3 vertices of contact; (b) 2 vertices of contact; (c) a group of 8 wire rings

Fig. 12. The rockfall impact test on a flexible ring net: (a) setup of physical model test; (b) the DEM model

Fig. 13. The three-dimensional and lateral view of net deformation for the impact test

Fig. 14. Comparison of DEM simulation values with FEM and experimental results of the flexible ring net under the rockfall impact: the evolution with time of the rockfall acceleration: (a) 12 turns per wire ring; (b) 7 turns per wire ring; (c) 19 turns per wire ring